GPS/INS Integration with Fault Detection and Exclusion in Shadowed Environments

Benjamin J. Clark
Samuel Ginn College of Engineering
GPS and Vehicle Dynamics Lab
Auburn University
Auburn, Alabama 36849
Email: clarkbj@auburn.edu

David M. Bevly
Samuel Ginn College of Engineering
GPS and Vehicle Dynamics Lab
Auburn University
Auburn, Alabama 36849
Email: bevlydm@auburn.edu

***Abstract*—This paper presents a method for GPS/INS operation in shadowed environments such as urban canyons and rural foliage cover. Shadowing causes a combination of multipath and signal attenuation which results in increased uncertainty in the GPS observables and sometimes complete loss of satellite tracking. Environment layout and the line-of-sight vector to the affected satellite determines the degree of shadowing in the range domain. Details are provided for the failure modes and effects in such environments. These results are used in the analysis of a fault detection and exclusion (FDE) algorithm to provide integrity to the GPS observables.**

Also, a closely coupled GPS/INS integration is described in which inertial measurements are combined with available GPS ranges even when less than four satellites are in view; a common difficulty in shadowed environments. By using the raw GPS observables in the integration, GPS information is still available for aiding even during severe loss of satellite visibility. The closely coupled integration method is chosen since raw range information is used in both the navigation solution and the FDE algorithm.

Using the closely coupled system with an FDE algorithm provides persistent position estimation. Solutions are available even when a stand-alone GPS solution could not be provided; a necessity in position critical applications. It is shown that the effects of shadowed environments can be detected and mitigated and still navigated through the use of inertial coupling with FDE.

I. Motivation

This research is being pursued in conjunction with vehicle navigation and control in various environments, particularly heavy tree cover. The GPS's global availability and long-term accuracy make it theoretically ideal for this type of system. However, GPS operation in certain environments can be greatly degraded. These harsh environments provide special challenges to GPS receivers. In order to successfully control the desired system, continuous operation is required. This is often not possible for stand-alone receivers. The resulting navigation system is designed to provide road-level accuracy, which is accuracy on the order of a meter. It will also meet other design requirements including low additional system cost, continuous availablity, and operation in heavy foliage.

To illustrate the difficulty of using a stand-alone GPS receiver in heavy foliage, a commercial receiver was used in a rural neighborhood in Auburn, Alabama, USA. Figure 1 shows the positioning of a NovAtel DL-V3 receiver operating in relatively dense tree cover. As can be seen, position jumps on the order of tens of meters occur in this wooded area. Also, due to satellite blockages, there are segments for which there is insufficient data to calculate a user position. These effects are similar to those experienced in urban canyon environments. This performance shows that a need exsits for both augmentation of a stand-alone receiver and the capability to detect and mitigate errors created in these environments.

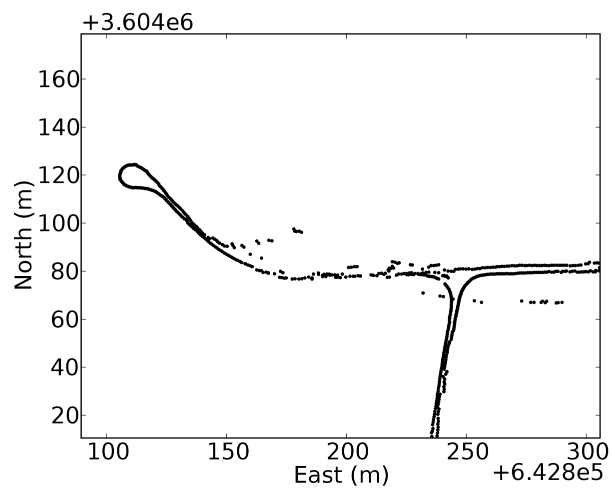

Fig. 1. NovAtel Reported Position

A. Shadowed Environments

In the literature areas blocking satellite visibility are called shadowed environments [1]. These environments are subject to some sort of signal blockage that degrades receiver performance. Some examples of these environments are heavy foliage, urban canyon, and indoor areas. As has been studied in many cases, all users of the GPS are exposed to several common errors [2]. These include errors in the broadcast ephemeris, signal delays from atmospheric effects like the ionosphere and troposphere, multipath, and receiver thermal noise. Users in shadowed environments suffer from these error modes but are also exposed to other local effects. These include signal blockages where a receiver is unable to track a satellite due to an obstacle blocking the line-of-sight, quickly changing multipath due to a large number of objects in close proximity, and signal attenuation due to interfering objects. These are the main effects considered in this research.

II. Analysis

In order to study how these error sources were occuring in heavy foliage environments, monitoring methods were investigated. To determine signal attenuation effects the carrier-to-noise ratio ($\mathrm{C/N_0}$) monitored. This gives information as to when a signal is degraded but loss-of-lock has not occurred. To monitor multipath, observation of a parameter $MP1$ is shown to be related to a receiver's pseudorange multipath [3]. Calculation of this variable requires L1 pseudorange and L1 and L2 carrier phase measurements. Therefore static dual-frequency data was collected using a NovAtel DL-V3 receiver. The photo in Figure 2 shows the location of the static analysis since it provided a good contrast between clear view and heavy foliage. This allowed for clear distinctions between the two environments to be drawn. A visualization technique was then used to evaluate these effects in heavy foliage. With this analysis, some decisions were made to simplify the overall system design.

Fig. 2. Static Data Collection Location

A. Error Source Monitoring

Signal attenuation arises when the signal passes through foliage cover. These obstacles cause both a delay and a reduced signal amplitude which increases the difficulty of tracking the signal. This reduced amplitude effect can be seen in the $\mathrm{C/N_0}$ that is reported by the GPS receiver. Decreases in the $\mathrm{C/N_0}$ increase the receiver's delay-locked-loop uncertainty, σ_{tDLL}, shown in Equation 1. This uncertainty is determined by receiver tracking loop architecture and values were taken from [4] and shown in Table I. The pseudorange variance, σ_ρ^2, is the combination of the tracking error and the atmosphere errors shown in Equation 2. This atmosphere variance is taken from the GPS error budget found in [5]. It is asumed to take a constant value of $\sigma_{atm} = 5.22$ m.

$$\sigma_{tDLL} = \lambda_c \sqrt{\frac{4F_1 d^2 B_n}{\mathrm{C/N_0}}\left(2\,(1-d) + \frac{4F_2 d}{T\mathrm{C/N_0}}\right)} \tag{1}$$

$$\sigma_\rho^2 = \sigma_{tDLL}^2 + \sigma_{atm}^2 \tag{2}$$

TABLE I
DLL Parameters

Parameter	Value	Units
F_1, discriminator correlator factor	1	-
F_2, discriminator type factor	1	-
d, correlator spacing	$\frac{1}{2}$	chips
B_n, code loop noise bandwidth	2	Hz
T, predetection integration time	2	ms
λ_c, code chip width	293.05	m

The other dominant effect to monitor is multipath. Multipath occurs when multiple instances of the same signal arrive at the receiver antenna by reflecting off of one or more objects, as shown in Figure 3. The receiver attempts to track the combination of all copies of the signal, leading to decreased performance. Since the reflected path is always longer than the direct path, the multipath signals are always delayed. They are also typically weaker than the line-of-sight signal depending on the nature of the reflection. As seen in Figure 3, multipath often causes a large change in the line-of-sight to the signal source. This error mode also affects the receiver's range rate measurement since the antenna's velocity projected onto the line-of-sight vector to the satellite is different than its projection onto the reflected path.

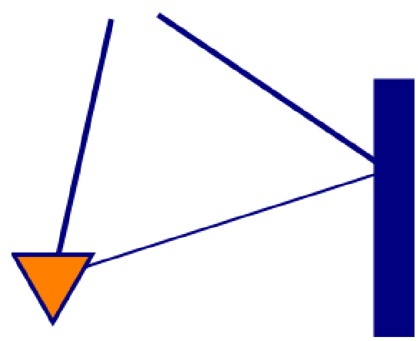

Fig. 3. Multipath Diagram

In order to quantify these multipath effects, a multipath monitoring variable is used. For a given satellite, three measurements are used to derive the $MP1$ parameter: the L1 pseudorange and L1 and L2 carrier phase. These measurements are shown in their common form with the error sources being added to the true range in Equations 3 and 4 with $i = 1, 2$, representing L1 and L2, respectively. The pseudorange, ρ_i, includes the satellite clock bias, cdt, receiver clock bias,cdt_u, ionosphere error, I_i, troposphere error, T_i, and multipath, $MP\rho_i$. Similarly, the carrier phase, ϕ_i, includes these errors and the carrier wavelength integer ambiguity, $\lambda_i N_i$. It should be noted that the multipath on the carrier phase, $MP\phi_i$, is significantly less than the multipath on the pseudorange [3].

$$\rho_i = r_i + c\,(dt - dt_u) + I_i + T_i + MP\rho_i \tag{3}$$

$$\phi_i = r_i + c\,(dt - dt_u) + \lambda_i N_i - I_i + T_i + MP\phi_i \tag{4}$$

The $MP1$ variable is calculated as a linear combination of dual-frequency measurements as shown in Equation 5 where $\alpha = \left(\frac{f_1}{f_2}\right)^2$. From derivations in [3], the multipath variable includes the L1 multipath on the pseudorange and carrier phase measurements ($MP\rho_1$ and $MP\phi_1$ respectively) and a bias term, B_1, as is shown in Equation 6.

$$MP1 = \rho_1 - \left(1 + \frac{2}{\alpha - 1}\right)\phi_1 + \left(\frac{2}{\alpha - 1}\right)\phi_2 \tag{5}$$

$$= MP\rho_1 + B_1 + MP\phi_1 \approx MP\rho_1 + B_1 \tag{6}$$

The bias is a function of the integer ambiguities and can be found explicitly as

$$B_1 = -\left(\lambda_1 N_1 - \lambda_2 N_2\right) - \lambda_1 N_1 - \frac{\lambda_1 N_1 - \lambda_2 N_2}{\alpha - 1} \tag{7}$$

This term can be removed by averaging or taking the first $MP1$ measurement as the bias term [3]. For this work, the change in multipath is being monitored so calculating the difference between successive $MP1$ variables removes the bias term. This approximates the change in L1 pseudorange multipath which is the effect to be monitored. Since B_1 is a function of the integer ambiguities, if a cycle slip occurs, an change in the bias will also occur. This would appear as a spike in the $MP1$ variable. This effect is neglected in the analysis but is a source of additional error.

B. Error Visualization

Both these monitoring variables can be plotted together to visualize the signal error at a point in time. For a single satellite, this is shown in Figure 4. The change in $MP1$ is shown as the magnitude in this error plot. The $\mathrm{C/N_0}$ is shown as the color in the plot. These effects together reveal the effects of the environment on the signal. This plot shows these monitoring variables for a single satellite signal as it passes from heavy foliage to a clear sky view. This diagram shows that the signal strength drops and multipath jumps correspond with each other, although not directly.

For a better view of what happens in tree cover, the static location discussed earlier was used. This location had heavy tree cover on the west side and clear sky on the east side. The overhead view of this area is shown in Figure 5. The combination of all satellite's monitoring variables are shown in Figure 6. This plot is similar to Figure 4 except that each of the $MP1$ and $\mathrm{C/N_0}$ plots are bent to follow the path that the satellite travels across the sky. This allows spatially correlated effects to be shown. Since there is a relatively distinct dividing line between the two regions, the distinction can also be drawn in the sky plot of Figure 6. This plot shows the effect that foliage has in quickly changing the multipath as well as degrading the signal. Low-elevation effects are also shown as

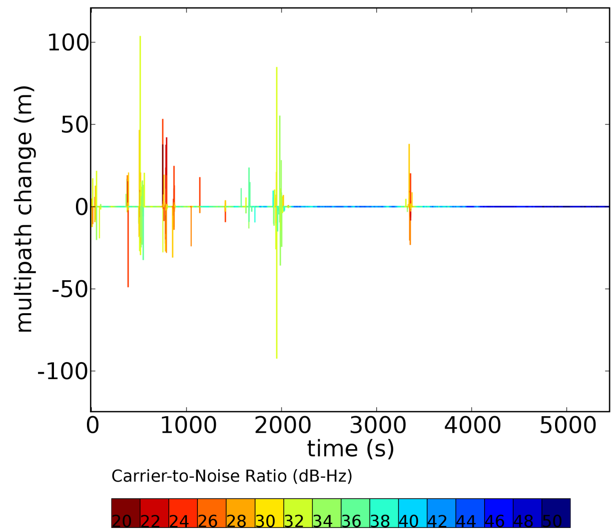

Fig. 4. Single Satellite Error Visualization

satellites get close to the outer circle. This plotting scheme is based off of [6] where only the actual multipath is plotted with respect to satellite azimuth and elevation. The visualization presented here shows the changing effects of the multipath as well as the signal strength for analysis in changing conditions.

Fig. 5. Aerial View of Static Data Location

III. Implementation

Now with this error analysis of shadowed environments, some decisions can be made about the desired navigation system. From the design requirements in Section I, the system must be low cost, operate continuously, and avoid solution

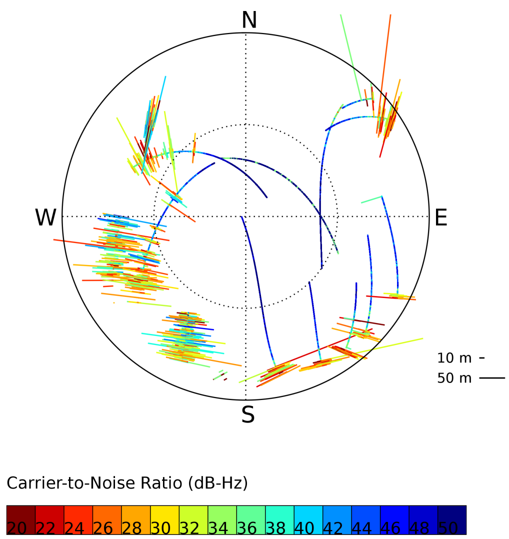

Fig. 6. All-In-View Satellite Error Visualization

spikes so that it can be used in conjunction with a vehicle controller. From the previous analysis, GPS alone will not meet these requirements. Thus, integration with an inertial sensor was used. The chosen implementation included integration with an inertial sensor in a closely coupled architecture with fault detection and exclusion (FDE) performed by an innovation monitoring technique.

A. Coupling Architectures

For this system, three coupling architectures found in the literature were considered [7]. These are shown in Figure 7. The IMU mechanization equations propagated the state and the overall solution is six degrees of freedom. The differences in the considered architectures come from what measurements are used by the coupling filter and whether or not the GPS receiver is aided by the filter. In a loosely coupled approach, the receiver calculates a solution using at least four satellites and its position and velocity are used as measurments. This solution is independent of the coupling solution. One major disadvantage of this method is that when the receiver cannot track enough satellites to compute the independent solution, the aiding measurements are not available. Therefore the coupled solution accuracy is determined by the drift characteristics of the low-cost IMU. In the closely coupled architecture, pseudorange and pseudorange rate are used as measurements, thus updating is continued with less than 4 satellites. In this case, the GPS position calculation is moved into the coupling filter rather than being performed independently. Finally, a tightly coupled system also uses pseudorange and pseudorange rate measurements but aids the receiver in tracking. This approach increases the capabilities of tracking in GPS harsh environments, particularly dynamic maneuvers. However, it requires the use of a GPS receiver that can accept the aiding measurements. The nomenclature for these methods has changed over time but these labels effectively delineate the architecture being used. For this work closely coupled is chosen since it continuously updates errors but does not require GPS hardware that can take aiding information.

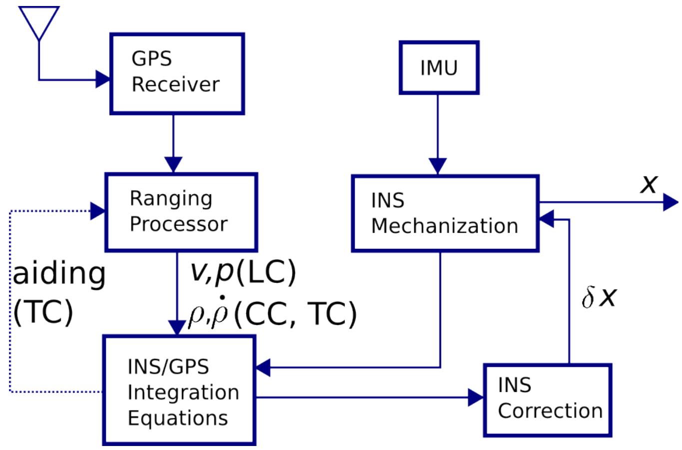

Fig. 7. Coupling Architectures

B. INS Mechanization Equations

The GPS/INS integration scheme includes 17 states used to keep track of the vehicle's motion, shown in Equation 8. These states are partitioned into six groupings of similar variables. For these equations, a superscript represents the coordinate frame the components are reported in and subscripts describe which frame origins the variable represents. The frames mentioned in this paper are the inertial frame, i, the Earth-Centered-Earth-Fixed (ECEF) frame, e, the navigation frame, n, and the body frame, b. Detailed descriptions of these frames are provided in [8]. The state vector includes three components of attitude error, ψ^e_{eb}, which are used to update the coordinate transformation matrix from body to ECEF frames, C^e_b; three components of velocity error in the ECEF frame, v^e_{eb}; and three components of position error in the ECEF frame, r^e_{eb}. The three accelerometer biases, b_a, and three gyro biases, b_g, are included and modeled as constants with process noise. The receiver clock bias, cdt_u, and drift, $c\dot{d}t_u$, are included with the clock drift modeled as a constant.

$$x = \begin{bmatrix} \delta\psi^e_{eb} \\ \delta v^e_{eb} \\ \delta r^e_{eb} \\ b_a \\ b_g \\ cdt_u \\ c\dot{d}t_u \end{bmatrix} \tag{8}$$

The coupling algorithm uses the corrected INS state solutions. The IMU inputs of angular rates, $\omega^b_{ib} = [\, g_x \quad g_y \quad g_z \,]^T$, and specific force, $f^b_{ib} = [\, f_x \quad f_y \quad f_z \,]^T$, are used to drive these states as shown in Equations 9 - 12. With Ω^b_{ib} being the skew-symmetric form of the angular rate vector ω^b_{ib}, and Δt the IMU measurement time step, the rotation matrix is propagated as [8]

$$C_b^e = C_b^e \cdot \left(I_3 + \Omega_{ib}^b \Delta t\right) - \left(\Omega_{ie}^e \cdot C_b^e\right) \Delta t \tag{9}$$

The specific force vector is translated to the ECEF frame by

$$f_{ib}^e = C_b^e \cdot f_{ib}^b \tag{10}$$

With the acceleration due to gravity and earth rotation given as g_b^e, the velocity state is propagated as

$$v_{eb}^e = v_{eb}^e + \left(f_{ib}^e + g_b^e - 2\Omega_{ie}^e \cdot v_{eb}^e\right) \Delta t \tag{11}$$

The position vector can then be updated as

$$r_{eb}^e = r_{eb}^e + v_{eb}^e \Delta t \tag{12}$$

C. State Dynamics

In order to use the coupling architecture in Extended Kalman Filter form, the equations given in Section III-B are linearized for propagation of the state errors, δx and its error covariance matrix, P. The form of the state equation is

$$\dot{\delta x} = F \delta x + w_s \tag{13}$$

where

$$F = \begin{bmatrix} -\Omega_{ie}^e & O_3 & O_3 & O_3 & C_b^e & O_2 \\ F_{21} & -2\Omega_{ie}^e & F_{23} & C_b^e & O_3 & O_2 \\ O_3 & I_3 & O_3 & O_3 & O_3 & O_2 \\ O_3 & O_3 & O_3 & O_3 & O_3 & O_2 \\ O_3 & O_3 & O_3 & O_3 & O_3 & O_2 \\ O_2^T & O_2^T & O_2^T & O_2^T & O_2^T & F_{66} \end{bmatrix} \tag{14}$$

$$F_{21} = \begin{bmatrix} 0 & -f_z & f_y \\ f_z & 0 & -f_x \\ -f_y & f_x & 0 \end{bmatrix} \tag{15}$$

$$F_{23} = \frac{2g_0}{r_{en}^{e2}} \frac{r_{eb}^e r_{eb}^{eT}}{|r_{eb}^e|} \tag{16}$$

$$F_{66} = \begin{bmatrix} 0 & 1 \\ 0 & 0 \end{bmatrix} \tag{17}$$

where I_m represents an identity matrix of size $m \times m$, O_3 represents a 3×3 null matrix, O_2 is a 3×2 null matrix, and w_s is the process noise included in the sytem derivation.

The state transition matrix at the current time step, k, can be approximated as

$$\Phi_k = I_{17} + F \Delta t \tag{18}$$

This allows for the propagation of the state correction as

$$\delta x_k^- = \Phi_k \delta x_{k-1}^+ \tag{19}$$

With the state transition matrix, the covariance matrix can be updated to

$$P_k^- = \Phi_k P_{k-1}^+ \Phi_k^T + Q \tag{20}$$

Where Q is the system noise covariance matrix which is assumed to be a diagonal matrix with entries given in Table II. These values were tuned to achieve the desired performance.

TABLE II
SYSTEM NOISE COVARIANCE MATRIX VALUES

State	Value	Units
Attitude Errors	0.01	rad/s
Velocity Errors	0.01	m/s
Position Errors	0.0005	m
Accelerometer Bias Errors	0.000001	m/s^2
Gyro Bias Errors	0.000001	rad/s
Clock Bias Error	0.1	m
Clock Drift Error	0.01	m/s

D. State Measurement Relations

The GPS/INS integration scheme uses measurements from all available satellites to update the state corrections as

$$z = H \delta x + w_m \tag{21}$$

where H is the state-measurement matrix and w_m is the measurement error included for derivation.

For satellite s, the pseudorange, ρ_s, and pseudorange rate, $\dot{\rho}_s$, measurements are used from the receiver. The rate measurement comes from the receiver's Doppler frequency measurement, f_{Ds}. This measure is transformed to a rate measurement as

$$\dot{\rho}_s = -\frac{c}{f_{L1}} f_{Ds} \tag{22}$$

where c is the speed of light and f_{L1} is the L1 carrier frequency.

Estimates of these measurements are given by the corrected INS solution, which is the system's best estimate of the state just before the measurement. These estimated pseudorange and pseudorange rate measurements are calculated as

$$\hat{\rho_s} = \sqrt{\left(r_{eb}^e - r_{es}^e\right)^T \cdot \left(r_{eb}^e - r_{es}^e\right)} + c dt_u \tag{23}$$

$$\hat{\dot{\rho}}_s = \frac{\left(r_{eb}^e - r_{es}^e\right)^T \cdot \left(v_{eb}^e - v_{es}^e\right)}{\sqrt{\left(r_{eb}^e - r_{es}^e\right)^T \cdot \left(r_{eb}^e - r_{es}^e\right)}} + c\dot{dt}_u \tag{24}$$

The differences in these measured and estimated quantities gives the measurement innovations which are used both to correct the state estimates and to run the fault detection and exclusion algorithm. These innovations are calculated as

$$\delta z_{\rho_s} = \rho_s - \hat{\rho}_s \tag{25}$$

$$\delta z_{\dot{\rho}_s} = \dot{\rho}_s - \hat{\dot{\rho}}_s \tag{26}$$

Placing all of the innovations in a column vector gives the measurement vector as

$$z = \begin{bmatrix} \delta z_{\rho_1} \\ \vdots \\ \delta z_{\dot{\rho}_1} \\ \vdots \end{bmatrix} \tag{27}$$

The integration equations use a standard Extended Kalman Filter algorithm with states desribed in Equation 8. The system is placed in linear form by differentiating the estimated measurements in Equations 23 and 24 with respect to each of the states. Approximations for this measurement state relationship matrix are made in [8] and are used here. For each row corresponding to a pseudorange, the resulting H matrix entry is

$$H_{\rho_s} = [\,O_3 \quad O_3 \quad u_{su} \quad O_3 \quad O_3 \quad 1 \quad 0\,] \tag{28}$$

where u_{su} is the unit vector from the satellite s to the user. Similarly, for each row corresponding to a pseudorange rate, the resulting H matrix entry is

$$H_{\dot{\rho}_s} = [\,O_3 \quad u_{su} \quad O_3 \quad O_3 \quad O_3 \quad 0 \quad 1\,] \tag{29}$$

Assuming uncorrelated measurements, the variances of these measurements are used as entries along the diagonal of the measurement covariance matrix R. The variance for a pseudorange measurement is described in Equation 2. The variance for a pseudorange rate measurement is assumed to be a function of the frequency-lock-loop (FLL) that generates the Doppler frequency measurement used in Equation 22. It is therefore taken from values given in [9] where the FLL thermal variance is taken to be

$$\sigma_{tFLL} = \frac{\lambda_L}{2\pi T}\sqrt{\frac{4FB_n}{\mathrm{C/N_0}}\left[1 + \frac{1}{T\mathrm{C/N_0}}\right]} \tag{30}$$

with parameters defined by the tracking loop architecture, shown in Table III. The Doppler frequency variance is then

TABLE III
FLL PARAMETERS

Parameter	Value	Units
F, loop factor	1	-
B_n, loop noise bandwidth	2	Hz
T, predetection integration time	5	ms
λ_L, carrier wavelength	0.1903	m

$$\sigma_{\dot{\rho}} = \sqrt{\sigma_{tFLL}^2 + \frac{f_e^2}{9}} \tag{31}$$

where f_e is the dynamic stress error, taken to be 3 m/s. At a given time step, if a set measurements are available, the measurement innovation vector, z, is generated and the Kalman gain calculated as

$$K = P_k^- H^T \left(HP_k^- H^T + R\right)^{-1} \tag{32}$$

Lastly, the state error and covariance matrix are updated using the measurements.

$$\delta x_k^+ = \delta x_k^- + Kz \tag{33}$$

$$P_k^+ = (I_{17} - KH)\, P_k^- \tag{34}$$

E. Fault Detection and Exclusion

Fault detection refers to the ability of a system to determine if there is a significant degradation in the GPS solution. The user is alerted if the system cannot guarantee solution accuracy to a certain level [8]. Fault exclusion provides a means to remove the fault and continue operation with the desired accuracy without having to alert the user. These schemes are used for critical applications where GPS availability and accuracy are necessary, such as aircraft landings. Traditionally these methods are used to detect and correct satellite failures. In this study, the errors being studied cause sporadic measurement outliers due to tree cover. Therefore the techniques are used to exclude outlying measurements and provide a more robust solution.

Since the errors in multipath and signal attenuation affect the receiver measurements and these errors enter the solution through the innovation, the innovation was chosen as the detection parameter. However, since the innovation is a function of measurement noise and not just these errors, jumps might not necessarily imply fault. A normalization routine gives more consistent operation. Each innovation is normalized by the square root of the C matrix diagonal, where $C = HPH^T + R$. The C matrix is calculated as part of Equation 32 and therefore does not increase the computational burden much. Thus, the normalized innovation is

$$y_i = \frac{z_i}{\sqrt{C_{ii}}} \tag{35}$$

These parameters are compared to a previsouly determined threshold, y_t. The measurement and its corresponding rows in the H and R matrix are removed if it is faulty, i.e. $y_i > y_t$. Currently the threshold value is taken from results found in [8] with a unitless value of 3. This value allows for the rejection of fairly drastic outliers while still using much of the information during normal operation. Further analysis is needed to validate other thresholds for operation.

IV. RESULTS

To test the system, a path was chosen to include clear and heavy foliage areas, shown in Figure 8. The route was located in Auburn, AL and began along a relatively clear roadway, shown in the top of Figure 9. Near the southern portion of the path, the test included heavy foliage shown at the bottom of Figure 9 that degraded signal accuracy and satellite visibility, even dropping to only one satellite being reported by the GPS receiver. This path was chosen to test the system in varrying conditions and to compare the system with stand-alone GPS solutions.

As a baseline comparison, only the reported L1 pseudoranges and satellite positions from broadcast ephemerides were used to calculate the receiver position. This standard least-squares algorithm calculates user ECEF position and clock bias [9]. Due to the foliage conditions, there were points at which no solution could be generated since too few satellites were reported. As is clear from Figures 10 and 11, this solution is unacceptable for position critical vehicle operations since

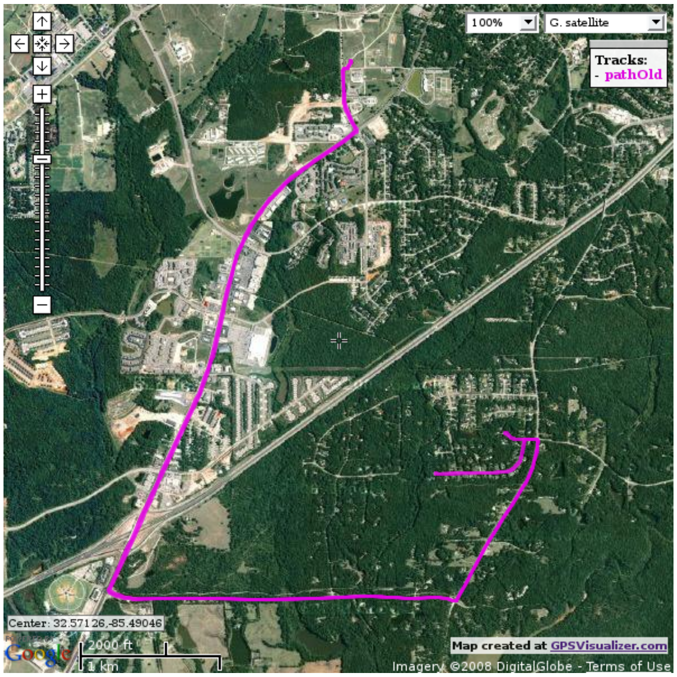

Fig. 8. Dynamic Path

Fig. 9. Environments Encountered

position jumps on the order of 100 meters occurs in several places.

A. Closely Coupled Implementation Results

Using the closely coupled algorithm by including the IMU allows the navigation system to bridge GPS signal degradation. For this implementation an automotive-grade IMU was used, the Xbow 440. It also increases the system solution rate to 50Hz, which is beneficial for vehicle control. The solution improves over the pseudorange position since the effect of

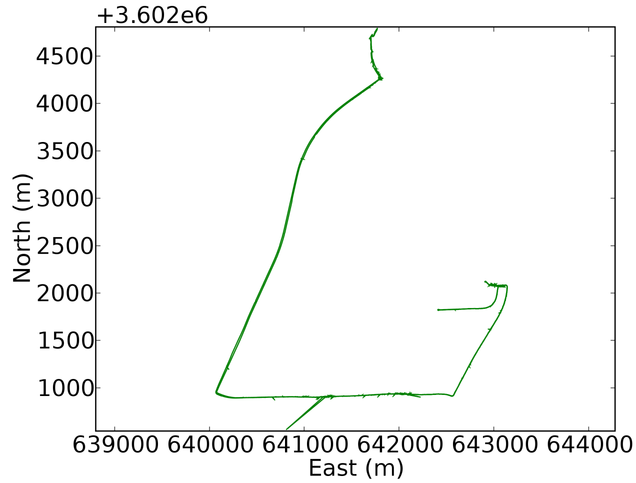

Fig. 10. Pseudorange Calculated Positoins

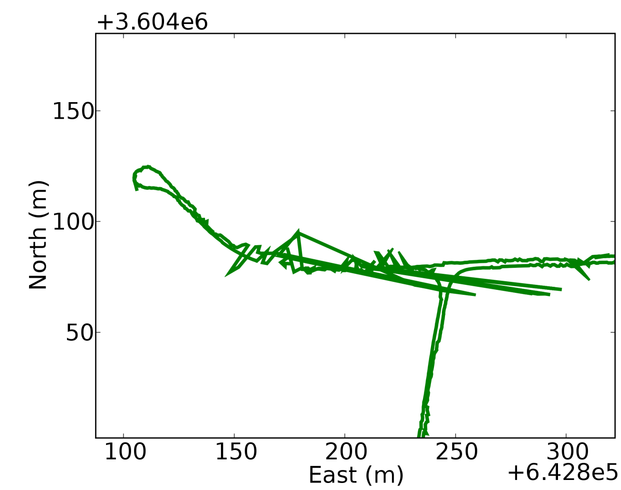

Fig. 11. Zoom on Pseudorange Calculated Positions

jumps due to foliage is filtered out, as seen in Figure 12. However, the solution still suffers from position and velocity jumps due to tree cover errors on the GPS measurements. These appear as the innovation outliers and their effect can be seen along the straight southern portion of the path shown in Figure 13. Here a satellite is reported at a single time epoch and its innovation is large compared to the other measurements. It pulls the velocity solution away which propagates to the jump in position solution.

B. Closely Coupled with FDE Implementation Results

By including the normalized innovation monitoring, these erroneous jumps are removed as shown in Figure 14. This implies that the correct outlier was detected and removed from the solution. As can be seen, this system is able to bridge parital signal loss while still estimating state corrections. These preliminary results show that the method is quite robust for operation in foliage environments like those encountered in

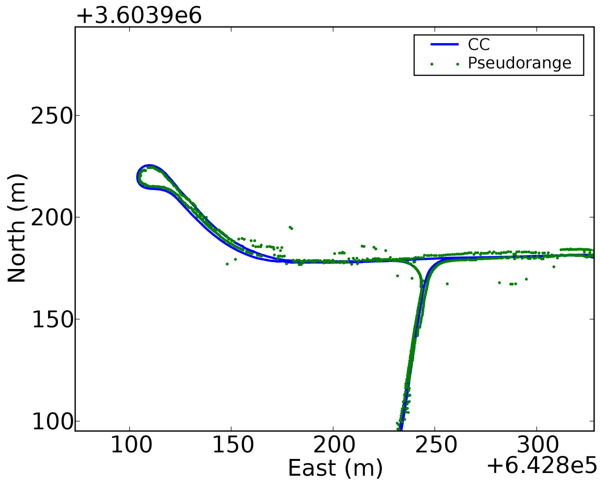

Fig. 12. Zoom on Closely Coupled Positions

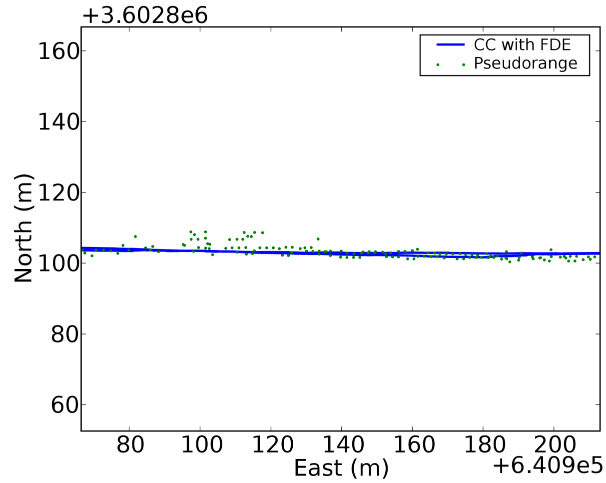

Fig. 14. Closely Coupled with FDE Results

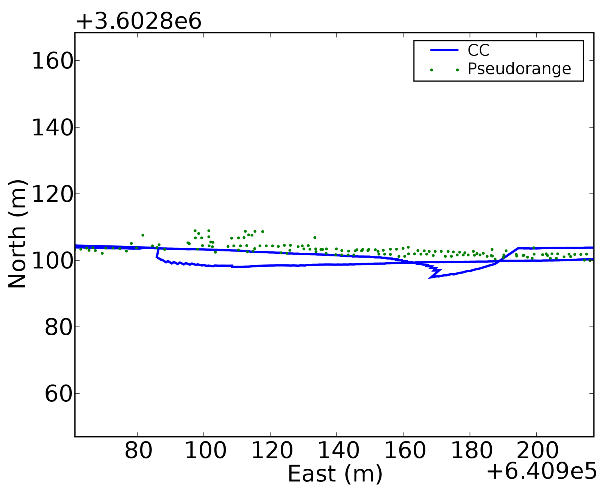

Fig. 13. Closely Coupled Results

the test path.

V. Conclusions

In conclusion, this work provides some insight into the errors affecting GPS operation in shadowed environments, specifically heavy foliage. It also details a visualization scheme for analyzing multipath changes and signal attenuation effects. It also presents a method of operation in these environments by implementing GPS/INS integration in a closely coupled architecture. Presented preliminary results show that this method fits design requirements for the desired operation of this system.

Acknowledgment

We acknowledge TARDEC for their support of this research.

References

[1] J. J. S. Jr., "Foliage attenuation for land mobile users," in *Global Positioning System: Theory and Application, Volume 1*. American Institute of Aeronautics and Astronautics, Inc., 1996.

[2] J. S. Jr., "Gps signal structure and theoretical performance," in *Global Positioning System: Theory and Application, Volume 1*, ser. Progress in Astronautics and Aeronautics, B. W. Parkinson and J. J. S. Jr., Eds. Washington, DC: American Institute of Aeronautics and Astronautics, Inc., 1996, vol. 163, ch. 3.

[3] C. Rocken, C. Meertens, B. Stephens, J. Braun, T. VanHove, S. Perry, O. Rudd, and M. M. J. Richardson, "Unavco academic research infrastructure (ari) receiver and antenna test report," UNAVCO, Tech. Rep., 1996.

[4] H. Leppakoski, H. Kuusniemi, and J. Takala, "Raim and complementary kalman filtering for gnss reliability enhancement," in *Proceedings of the PLANS Conference*, 2006.

[5] B. W. Parkinson, "Gps error analysis," in *Global Positioning System: Theory and Application, Volume 1*, B. W. Parkinson and J. J. S. Jr., Eds. American Institute of Aeronautics and Astronautics, Inc., 1996.

[6] S. Hilla, "Plotting pseudorange multipath with respect to satellite azimuth and elevation," *GPS Solutions*, vol. 8, pp. 44–48, 2004.

[7] C. R. Hamm, I. Warren S. Flenniken, D. M. Bevly, and D. E. Lawerence, "Comparative performance analysis of aided carrier tracking loop algorithms in high noise/high dynamic environments," in *Proceedings of the ION GNSS*. Long Beach, CA: ION, September 2004.

[8] P. D. Groves, *Principles of GNSS, Inertial, and Multisensor Integrated Navigation Systems*. Artech House, 2008.

[9] E. D. Kaplan and C. J. Hegarty, Eds., *Understanding GPS: Principles and Applications*. Artech House, 2006.